

Parallel conduction channels in topological insulator thin films: Role of the interface layer and the band bending in the film

Sven Just,^{1,2,3,*} Felix Lüpke,^{1,2,†} Vasily Cherepanov,^{1,2} F. Stefan Tautz,^{1,2,3} and Bert Voigtländer^{1,2,3,‡}

¹*Peter Grünberg Institut (PGI-3), Forschungszentrum Jülich, 52425 Jülich, Germany*

²*JARA-Fundamentals of Future Information Technology*

³*IV. Institute of Physics A, RWTH Aachen, 52074 Aachen, Germany*

(Dated: June 26, 2022)

Topological insulator (TI) thin films can exhibit multiple parallel conduction channels for current transport. Beside the topological protected surface states (TSS) there can be other channels, i.e. the interior of the not-ideally insulating TI film, the interface layer and the substrate. It is a crucial task to minimize the influence of these parasitic parallel channels on the total current transport for taking advantage of the special properties of the TSS. We present a method for the determination of the conductivity of the interface between the substrate and the TI film by distance-dependent surface-sensitive four-probe measurements performed with a multi-tip STM using the example of the Te/Si(111)-(7×7) interface. Moreover, the conductivity of the interior of the TI thin film (bulk) is difficult to access by measurements. We propose here an approach for calculating the near-surface band bending and the mobile charge carrier concentration inside the TI thin film based on data from surface-sensitive measurements, e.g. (gate-dependent) four-point resistance measurements and ARPES. Usually the amount of unintentional dopants inside the TI thin film is unknown, but it turns out that in the thin-film limit the band-bending is largely independent on the dopant concentration. This allows to give an estimate of the total mobile charge carrier concentration and the conductivity of the interior of the TI thin film.

I. INTRODUCTION

Topological insulator materials are candidates for future electronic devices and might be used for low-power spintronics or quantum computing due to the special properties of their topological protected surface states (TSS), e.g. spin-momentum locking and prohibited direct backscattering [1, 2]. In recent years, the material compounds Bi₂Se₃, Bi₂Te₃ and Sb₂Te₃ belonging to the class of chalcogenide van-der-Waals thin films have appeared to be most promising for applications at room temperature due to their pronounced band-gap [1, 3]. However, for taking advantage of the topological properties the electrical current has to be predominantly transmitted through the TSS channel. In fact, for TI bulk crystals the parasitic parallel bulk conductance channel plays a significant role and can even surpass the current transport through the TSS, as studied recently [4, 5]. The influence of the bulk can be suppressed, if TI materials are grown as thin films on sufficiently low-conducting substrates. However, also in this case multiple parallel conduction channels participating in current transport can be present, as it is visualized in Fig. 1. Beside the TSS channel, the current can also flow through the interior of the not-ideally insulating TI film, through the potentially highly conductive interface layer between TI film and substrate and through the substrate itself.

So, it is an important task to design future devices based on topological material thin films in such a way that the portion of current transport through these parallel parasitic channels is minimized for benefiting mostly from the special topological properties of this material class. In order to minimize the parasitic effects, the conductivities of the parasitic channels in real grown TI thin films have to be known. However, it is very difficult

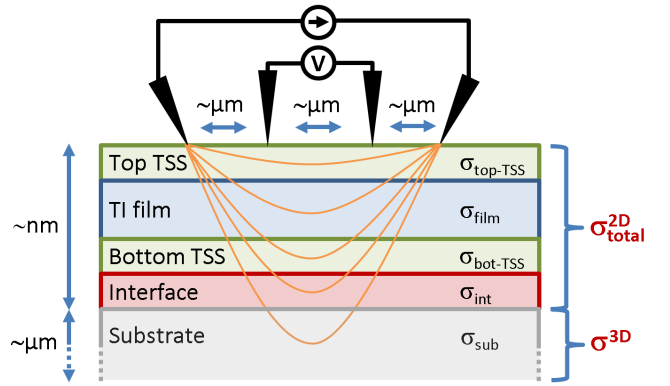


FIG. 1. (Color online) Multiple parallel conduction channels in a topological insulator thin film. The current transport can occur through the top and bottom TSS channel, but also through the interior of the TI film, through the interface layer between film and substrate as well as through the substrate itself. Position-dependent four-probe measurements on the surface can only differentiate between the total 2D conductivity, i.e. the sum of all parallel channels in the thin film, and the 3D substrate conductivity. Note that different from the schematic the film thickness (\sim nm) is much smaller than the usual distance between the tips (\sim μ m).

* Present address: Leibniz-Institut für Festkörper und Werkstofforschung Dresden, 01069 Dresden, Germany

† Present address: Department of Physics, Carnegie Mellon University, Pittsburgh, PA 15213, USA

‡ Corresponding author: b.voigtlaender@fz-juelich.de

to access these conductivities by electrical and surface-sensitive measurements due to the small thickness of the grown TI films on the order of 10 nm. This small scale prevents to use distance-dependent four-probe measurements on the surface to disentangle 2-dimensional (2D) from 3-dimensional (3D) conductance channels inside the thin film, as the probes would have to be spaced closer than one fourth of the film thickness, which is not reasonable, as this small spacing would approach the tip radius [6–10]. So, position-dependent surface four-probe measurements are only able to separate the total 2D conductivity of the TI thin film $\sigma_{\text{total}}^{2D}$, which is a composition of the top and bottom TSS, the TI film and the interface channels (Fig. 1), from the 3D substrate conductivity [6–10]. However, the substrate channel can easily be minimized by choosing an appropriate very low-doped substrate as template for the grown TI thin film.

Other methods are necessary to characterize the parasitic interface and bulk channels of a TI thin film. The interface conductance might be a result of a surface reconstruction of the substrate established at the beginning of the TI thin film growth and exhibiting a high density of states (DOS) at the Fermi energy in combination with a high mobility. If such a substrate reconstruction at the interface can be identified clearly, e.g. by transmission electron microscopy [11], and if the coupling to the TI film on top is rather small, which is the case for the commonly used van-der-Waals epitaxy, then there is the possibility to prepare only the reconstructed substrate without the TI film grown on top, enabling to determine the conductivity of the interface reconstruction by means of distance-dependent surface-sensitive four-probe measurements.

The interior of the TI film is more difficult to characterize, as it cannot be separated from the TSS channels on top and bottom side of the film. As the amount of unintentional dopants during TI film growth is not known properly, the charge carrier concentration and conductivity of the film material cannot be calculated directly. However, we will show here that in the thin-film limit a variation of the dopant concentration does not influence the mobile charge carrier concentration in the film in such a significant way, as it would occur in a corresponding half-infinite bulk crystal, where the doping effect would lead to a strong shift of the band edges with respect to the Fermi energy inside the bulk. In a thin film, this total shift of the bands with respect to the Fermi energy and the near-surface band-bending is much smaller due to the long screening length compared to the film thickness [12–14]. So, the mobile charge carrier concentration inside the thin film can be estimated independently of the exact amount of dopant concentration.

Here, we will present both methods for determining the conductivity of the two parasitic conductance channels, i.e. the interface layer and the interior of the TI thin film. First, the measurement method for the interface layer is discussed using the example of the Te/Si(111)-(7×7) surface reconstruction subsequently giving an overview for

conductivities of other possible interface reconstructions found in the literature. Second, detailed calculations of the band-bending in a TI thin film are presented for two different cases, i.e. for the approximation of a symmetric band-bending at both surfaces of the TI thin film and for the more general asymmetric case. The calculations use the properties of TI thin films, which are experimentally accessible by the surface-sensitive measurement methods angular-resolved photoemission spectroscopy (ARPES) and gate-dependent four-point resistance measurements. As an example, the calculations are applied to experimental data of a thin $(\text{Bi}_{1-x}\text{Sb}_x)_2\text{Te}_3$ film with $x = 0.5$ obtained from [15] and in the following referred to as BiSbTe₃.

II. INTERFACE CONDUCTION CHANNEL

A common substrate for growth of TI thin films by means of van-der-Waals epitaxy is Si(111). Here, an initial passivation of the surface dangling bonds at the beginning of the TI growth process results in a weak coupling of the on top grown TI film to the substrate by van-der Waals interaction [16–18]. However, such an interface reconstruction of the Si(111) can potentially have a high conductivity resulting in an additional channel for current transport beneath the TI thin film [9, 19–21]. The TI thin film exhibits a sharp interface on top of the Si(111) substrate, as deduced from scanning transmission electron microscopy [11, 18]. Due to the observed

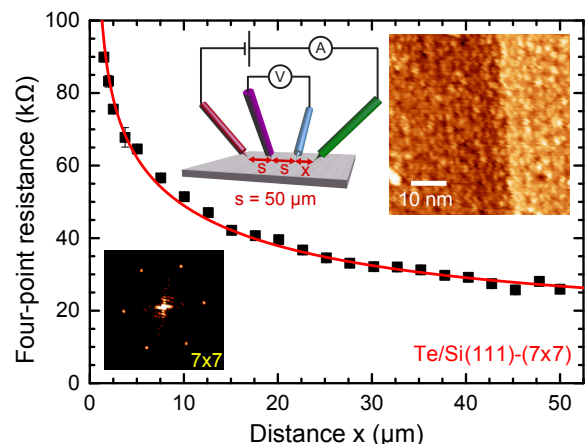


FIG. 2. (Color online) Measured four-point resistance of the Te/Si(111)-(7×7) surface reconstruction as function of the non-equidistant probe spacing x . The red line corresponds to a fit to the data using a pure 2D model according to Eq. 1 and results in a surface conductivity of $\sigma_{7\times7}^{\text{Te}} = (8.3 \pm 0.5) \cdot 10^{-6} \text{ S}/\square$. In the upper left inset, the probe configuration is visualized. The upper right inset shows a STM image of the Te/Si(111)-(7×7) surface exhibiting traces of the characteristic corner holes of the (7×7)-reconstruction. This periodicity can also clearly be seen by the distinct spots in the Fourier transformation of the STM image shown in the lower left inset.

large van-der-Waals gap the electronic properties of the TI thin film and the passivated substrate are largely decoupled. Particularly due to this decoupling it is possible to consider the conductivity of the substrate surface reconstruction without further grown TI thin film on top to be the same as the interface conductivity of the complete TI system. Therefore, it is sufficient to prepare only the Si passivation layer, in order to access the conductivity of the interface layer. The conductivity of this reconstruction can be investigated by surface-sensitive four-probe measurements.

For Te based van-der-Waals epitaxy, a possible interface reconstruction is the Te/Si(111)-(7×7) reconstruction, which is reported to be a template for the growth of TI thin films on Si(111) [3]. It can be prepared at room temperature by deposition of Te on top of a reconstructed Si(111)-(7×7) surface, which is described in the following. First, the (7×7)-reconstruction of the Si(111) substrate (p-doped, bulk resistivity 22.5 kΩcm) has to be established by heating up to 1200°C and subsequent slow decreasing of the temperature. Afterwards, the Si(111)-(7×7) surface is passivated by deposition of 1 ML Te at 300°C with a flux of 1 ML/min using a Knudsen cell. In subsequent low energy electron diffraction (LEED) measurements, weak (7×7) spots are visible (not shown here) indicating that some elements of the (7×7) structure are still present below the Te layer. Also in STM images the slightly appearing characteristic corner holes of the Si(111)-(7×7) reconstruction can be identified (upper right inset in Fig. 2). The corresponding periodicity can be seen more clearly by the distinct spots in the Fourier transformation of the STM image (lower left inset in Fig. 2) [22]. In order to determine the surface conductivity of the Te/Si(111)-(7×7) reconstruction distance-dependent four-probe measurements with a multi-tip STM at room temperature are performed with a linear non-equidistant tip configuration shown in the upper left inset of Fig. 2. The distance x between one outer current injecting tip and the adjacent inner voltage measuring tip is varied, while the spacing s between the other tips remains constant and is equal to $s = 50 \mu\text{m}$. With such a tip configuration the expected four-point resistance for a 2-dimensional sheet depends on the distances s and x , and can be described by [7, 11]

$$R_{2D}^{4p}(s, x) = \frac{1}{2\pi\sigma_{2D}} \left[\ln\left(\frac{2s}{x}\right) - \ln\left(\frac{s}{x+s}\right) \right]. \quad (1)$$

In Fig. 2 the measured four-point resistance of the Te/Si(111)-(7×7) surface is plotted as function of the spacing x . The solid red line corresponds to a 2D fit according to Eq. 1 showing a good correspondence to the data and results in a surface conductivity of $\sigma_{7\times 7}^{\text{Te}} = (8.3 \pm 0.5) \cdot 10^{-6} \text{ S}/\square$. This value is slightly higher compared to the conductivity of the pure Si(111)-(7×7) surface of $\sigma_{7\times 7}^{\text{Si}} = (5.1 \pm 0.7) \cdot 10^{-6} \text{ S}/\square$ [9]. So, in combination with the results from STM and LEED it can be concluded that the Si(111)-(7×7) reconstruction is still partly intact underneath the deposited Te and its conduc-

tivity is increased by the doping through the additional Te. However, if $\sigma_{7\times 7}^{\text{Te}}$ is for example compared to typical TSS conductivities of $\sigma_{\text{TSS}} \approx (4 - 8) \cdot 10^{-4} \text{ S}/\square$ [23, 24], only 1 - 2% of the total current would flow through the interface channel indicating that this channel does not play a significant role in the overall current transport.

A further interface termination is the Te/Si(111)-(1×1) reconstruction, which forms in fact the most common template for Te based van-der-Waals epitaxy, e.g. as used for the growth of Bi₂Te₃ [16]. The reconstruction exhibits a surface conductivity of $\sigma_{1\times 1}^{\text{Te}} = (2.6 \pm 0.5) \cdot 10^{-7} \text{ S}/\square$ [11], which is substantially lower compared to the conductivity of the Te/Si(111)-(7×7) surface. If this value is compared to typical TSS conductivities of $\sigma_{\text{TSS}} = (4 - 8) \cdot 10^{-4} \text{ S}/\square$, it turns out to be very small, so that the interface channel would contribute only less than 1% to the total current transport in the TI system and is therefore negligible.

For Bi based van-der-Waals epitaxy, a common template for TI thin film growth is the Bi/Si(111)-($\sqrt{3} \times \sqrt{3}$) surface reconstruction, which remains stable upon Te flux [3, 24-27]. The conductivity of this surface reconstruction is reported to be $\sigma_{\sqrt{3} \times \sqrt{3}}^{\text{Bi}} = (1.4 \pm 0.1) \cdot 10^{-4} \text{ S}/\square$ [9]. This value is in the range of the TSS conductivity σ_{TSS} , so that in this case a substantial amount (20 to 35%) of the total current through the TI system would be transmitted by the interface channel. Due to this high parasitic conductance, a Bi terminated interface of the Si(111) substrate exhibiting the Bi/Si(111)-($\sqrt{3} \times \sqrt{3}$) reconstruction would be not favorable for designing TI devices.

Very similar results as in the case of the Te/Si(111) interface terminations can also be expected for Se based van-der-Waals epitaxy on Si(111) [28-30]. However, exact values for the surface conductivities of the respective (1×1) and (7×7) reconstructions have not been reported in the literature. Furthermore, in the case of initial Se termination, additional amorphous interface layers up to several nm in thickness can occur depending on the preparation parameters [25, 31]. Such a thicker interface region can also have a significant effect on the interface conductivity, as it is now a superposition of the conductivities of the Se/Si(111) substrate surface reconstruction and the additional amorphous layers.

In conclusion, the interface conductivity can have a significant influence on the overall current transport in a TI thin film and strongly depends on the material system and preparation parameters. For the example of TI thin films grown by Te based van-der-Waals epitaxy, as Bi₂Te₃, Sb₂Te₃ and corresponding ternary/quaternary compounds, the Te/Si(111)-(1×1) interface reconstruction is the best choice, as it exhibits only a very low parasitic conductivity nearly not influencing the current transport through the TSS channel. However, potential high interface conductivity is a general problem not only for TIs but also for other van-der-Waals thin films and should therefore be determined individually for each material system.

III. BULK CONDUCTION CHANNEL

The second important parasitic conductance channel inside TI thin films is the non-vanishing film material (bulk) conductivity. In principle, the TI bulk should be insulating, as the Fermi energy is placed inside the bulk band gap with only the Dirac cone of the TSS crossing it, but due to unintentional doping during the growth process, there can be potentially a high bulk conductivity. This can result in a substantial amount of current flowing through the interior of the TI film rather than through the TSS, as it would be desired. In contrast to extended TI bulk crystals the film conductivity of TI thin films can be influenced very much by tailored film growth [16] and large surface-to-volume ratios, i.e. small thicknesses of the TI films in the order of 10 – 100 nm. However, often it is not possible to suppress the film bulk contribution to current transport completely. Furthermore, there is also an influence of the TSS on the top and bottom sides of the TI thin film on the film bulk conductivity due to charge transfer between the TSS and the interior of the film resulting in a near-surface band-bending and the formation of a space-charge region. So, it is necessary to have a closer look onto the film conduction channel in order to determine its contribution to the overall current transport in a TI thin film.

In the following, the TI thin film is modeled as a small bandgap semiconductor in order to calculate the near-surface band-bending induced by the top and bottom TSS in a semi-classical approach, including the quantization effect arising from the confinement of the electrons due to the small TI film thickness in the range of several nanometer. Hereby, the first one and a half iterations of the Schrödinger-Poisson approach are used as an approximation: Starting with Poisson's equation first the classical problem is solved. On the resulting band-bending potential the Schrödinger equation is applied to calculate the quantized eigenenergies forming multiple subbands inside the conduction and valence bands. This subbands result in a modification of the effective density of states used in another application of Poisson's equation for finally calculating the band bending and the mobile charge carrier densities inside the bands. Further calculation details are described in the following and can additionally found in the supplementary material [32].

In the following, first the simple case for a semi-infinite bulk crystal is discussed as reference, and secondly, the calculation for a thin film with two interfaces assuming symmetric boundary conditions, i.e. equal charge carrier density in top and bottom TSS, is presented. Thirdly, the more general case of asymmetric band-bending in a thin film is presented.

Within all equations and figures, the following notation is used: The Fermi energy E_F is aligned throughout the crystal and the bands are shifted with respect to the constant Fermi energy E_F . The position of the valence band edge $E_{VB}(z)$ with respect to the Fermi energy E_F at the top and bottom surface of the thin film and in-

side the bulk crystal is expressed by the variables E_F^{top} , E_F^{bot} and E_F^{bulk} , respectively. These variables are defined by the difference $E_F^{\text{top,bot,bulk}} = E_F - E_{VB}^{\text{top,bot,bulk}}$ and referred to as top and bottom surface Fermi energy and bulk Fermi energy, respectively.

A. Semi-infinite bulk crystal: near-surface band-bending

The general calculation of the near-surface band-bending in the classical approach is based on solving Poisson's equation $\Delta\Phi = -\rho/\epsilon_0\epsilon_r$ for the charge carrier concentration ρ in the space charge region assuming the Boltzmann approximation. The potential Φ is determined by $\Phi(z) = (E_F^{\text{bulk}} - E_{\text{intrinsic}}(z))/q$ and the band-bending can be expressed by $V(z) = \Phi(z) - \Phi_b$, where E_F^{bulk} and $E_{\text{intrinsic}}$ are the bulk Fermi energy and the intrinsic level, respectively, q is the elementary charge and the index b denotes the bulk value of the potential far away from the surface. For the calculation, specific material parameters are used as input, i.e. the band gap and the effective masses of electrons and holes, and a parabolic approximation of the bulk band edges is assumed in order to calculate the effective density of states. Introducing the dimensionless potentials $u(z) = q\Phi(z)/k_B T$ and $v(z) = qV(z)/k_B T$ with the temperature T and the Boltzmann constant k_B , Poisson's equation can be expressed by [33, 34]

$$\frac{d^2v}{dz^2} = -\frac{q^2}{\epsilon_0\epsilon_r k_B T} \cdot (n_b - p_b + p_b e^{-v} - n_b e^v) \quad (2)$$

with n_b and p_b denoting the charge carrier concentrations in the bulk for electrons and holes, respectively. Eq. 2 can be rearranged by using the Boltzmann approximation into

$$\frac{d^2v}{dz^2} = \frac{1}{L^2} \left(\frac{\sinh(u_b + v)}{\cosh(u_b)} - \tanh(u_b) \right) \quad (3)$$

with the effective Debye length $L = \sqrt{\epsilon_0\epsilon_r k_B T / q^2(n_b + p_b)}$ and integrated to

$$\frac{dv}{dz} = \text{sgn}(-v) \frac{\sqrt{2}}{L} \sqrt{\frac{\cosh(u_b + v)}{\cosh(u_b)} - v \cdot \tanh(u_b) + c} \quad (4)$$

with the constant c to be determined from the boundary conditions.

For a semi-infinite bulk crystal the boundary conditions are $\frac{dv}{dz} = 0$ for $v \rightarrow \infty$ and $v(0) = v_{\text{top}} = (E_F^{\text{top}} - E_F^{\text{bulk}})/k_B T$ with the index *top* denoting the potential value at the surface and the surface Fermi energy E_F^{top} . Inserting the boundary conditions into Eq. 4 and using the definitions of the hyperbolic functions leads to the solution [33, 34]

$$z(v) = A \int_{v_{\text{top}}}^{v(z)} \sqrt{\frac{e^{u_b} + e^{-u_b}}{e^{u_b}(e^v - v - 1) + e^{-u_b}(e^{-v} + v - 1)}} dv \quad (5)$$

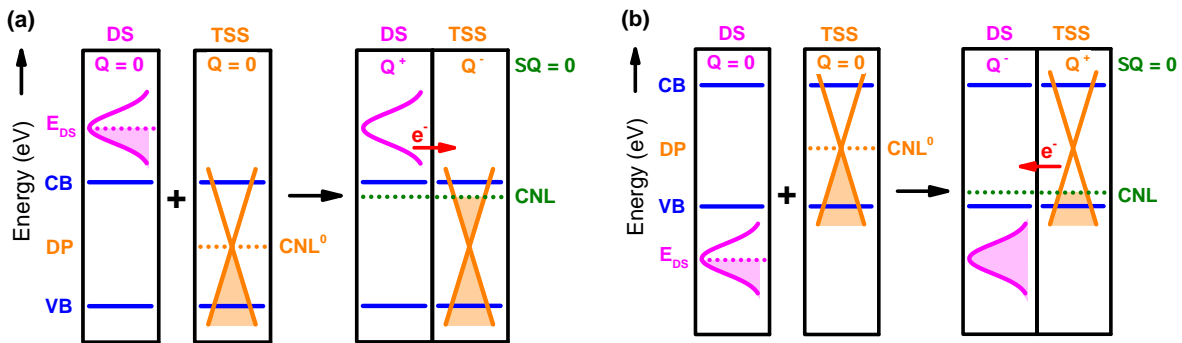


FIG. 3. (Color online) Principle of the formation of the CNL level in the TSS for the presence of additional trivial defect states (DS) exhibiting a finite amount of charge. Both the DS (magenta) located around E_{DS} and the TSS/Dirac cone (orange) are filled up to its individual charge neutrality levels (dotted lines), if they would be artificially separated from each other (left parts of (a) and (b)). However, if the DS and TSS are combined (right parts), a charge transfer occurs resulting in a different common aligned value for CNL for both (green line). This final CNL value is strongly influenced by the position of the DS (E_{DS}) being above (a) or below (b) the Dirac point.

with the prefactor $A = \text{sgn}(-v) \frac{L}{\sqrt{2}}$. Eq. 5 will be integrated and inverted numerically to determine the band-bending $v(z)$.

For several semiconductors the Fermi energy at the surface is pinned at a fixed position relative to the band edges due to a very high DOS of the semiconductor-surface states. In contrast, in TIs a relatively low DOS is caused by the presence of the Dirac cone of the TSS, so that the assumption of a pinned value of E_F^{top} is not true. The DOS of the TSS depends on the shape of the Dirac cone and by taking into account the linear dispersion of the Dirac cone $E(k) = \hbar v_F k$ [35] the amount of charge carriers inside can be written as function of energy with respect to an initial filling state E_0 , which might be caused by surface doping due to surface defects or adsorbates, as [15]

$$n_{\text{dc}}(E) = \frac{1}{4\pi\hbar^2 v_F^2} (E^2 - E_0^2). \quad (6)$$

Without the presence of surface defect states the Dirac cone is filled up to the Dirac point. The position of the filling level of the Dirac cone in a TI material, i.e. the surface Fermi energy, can be determined by surface-sensitive ARPES measurements, and afterwards used as a known parameter in the band-bending calculations in the same way as for semiconductors. However, an important point is that in TIs the surface Fermi energy is not pinned and can change its value due to several external influences, e.g. the amount of adsorbates on the surface, the bulk dopant concentration or the application of a gate voltage, as it will be discussed in more detail in the following. In contrast, the exact value for the bulk Fermi energy E_F^{bulk} is not known, as the exact amount of dopants in the bulk material is often unknown for TIs, so that E_F^{bulk} has to remain as a free parameter in the calculations.

For a more detailed understanding of the mechanism of near-surface band bending in TI materials, a closer look onto the parameters influencing the charge transfer

between the TSS and the bulk is necessary. In the same way as for semiconductors, the band bending is governed by the condition of charge equality with opposite sign between surface state and bulk. Conceptually, the filling of the surface states not yet connected to the bulk is compared to the filling level when connected to the bulk [36]. For TI materials, this implies that the filling of the Dirac cone changes between an initial level (not connected to the bulk) and a final level, when charge exchange with the bulk has occurred. The initial filling level of the Dirac cone is identified with the charge neutrality level (CNL), at which the TSS is neutral before the connection to the bulk, in the same way as it also applies for semiconductors [36]. In the framework of semiconductors this charge neutrality level (CNL) describes the filling level of the surface state, at which it is completely neutral, and correspondingly no band bending at the surface occurs upon the connection to the bulk (flat band condition). Thus, the CNL can also be described as the initial filling level, up to which the (neutral) surface state is filled before equilibration with the bulk. If this concept is transferred to a topological insulator, the initial filling and charging state of the TSS can be described in the same way by the CNL. Within this view, the TSS is first assumed to be separated from the bulk material, so that the CNL describing a completely neutral Dirac cone is rather a theoretical quantity and not directly measurable. Ideally, for a neutral and isolated TSS the Dirac cone is filled up to the Dirac point, so that Dirac point and CNL coincide.

However, the presence of additional trivial defect states (DS) on the surface of the TI can have a strong influence on the CNL and can induce a shift of the energy position of the CNL value. In this case, the surface doping caused e.g. by surface defects or additional adsorbates on the surface leads to a different filling level of the TSS in order to compensate the additional charges of the DS and fulfilling surface neutrality. So, in general the CNL of the combined TSS/DS system (considered as

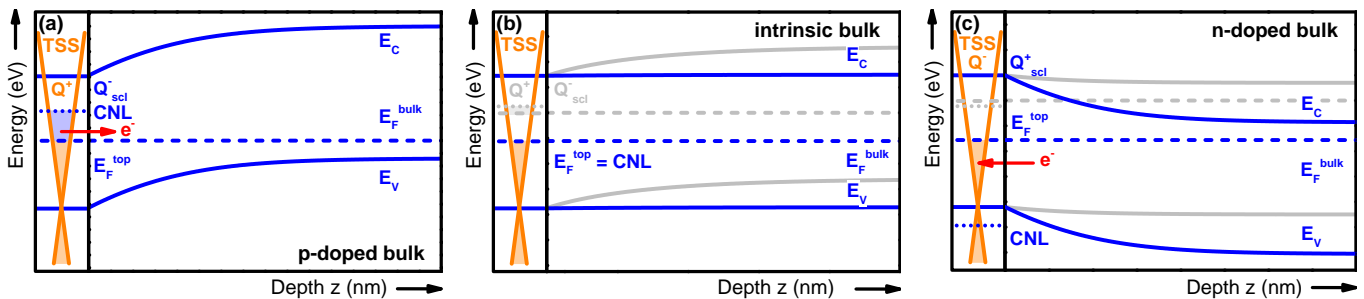


FIG. 4. (Color online) Principle of band bending in extended TI bulk crystals for three different bulk dopant concentrations, i.e. (a) p-doped, (b) intrinsic, and (c) n-doped, in combination with either specified values for the surface Fermi energy E_F^{top} or the charge neutrality level CNL of the TSS. On the left edge, the partially filled (highlighted orange area) Dirac cone of the TSS is shown, and on the right side the calculated conduction and valence bands are plotted as function of depth z into the crystal. The Fermi energy E_F is depicted as dashed line, while the relative position of the Fermi energy with respect to the valence band edge at the surface and inside the bulk is described by the values for the surface Fermi energy E_F^{top} and for the bulk Fermi energy E_F^{bulk} , respectively. For the blue band diagrams in (a)-(c) the surface Fermi energy E_F^{top} (which can be measured by ARPES) is assumed to have a constant midgap position resulting in different bending of the bands and different positions of the CNL according to the charge neutrality condition, if the dopant concentration (E_F^{bulk}) is varied. The CNLs are indicated by the dotted lines. The gray band diagrams in (b) and (c) exhibit the same bulk dopant concentrations as the blue diagrams, but now the CNL is assumed to be kept constant, resulting in different positions of E_F^{top} and in a different shape of band bending than in the blue colored cases.

isolated from the bulk) is not located at the Dirac point. The basic principle of the formation of the CNL due to defect-induced surface states (DS) is visualized in Fig. 3. The trivial DS (magenta) is assumed to exhibit a finite amount of charge due to a finite density-of-states (DOS) distributed in the vicinity of a fixed position E_{DS} with respect to the valence band edge (VB) (different values in Fig. 3(a) and 3(b)). Initially (before combination with the TSS), the DS is neutral and filled up to its charge neutrality level (dotted magenta line and highlighted area). The isolated Dirac cone of the TSS (orange) is also neutral and filled up to the Dirac point (DP) (highlighted area), which represents the initial CNL⁰ value (dotted orange line).

If the trivial DS and the TSS are combined (right parts of Fig. 3), a charge transfer occurs leading to an aligned value for the CNL (dotted green line). For a DS above the conduction band (CB), as shown in Fig. 3(a), electrons flow into the TSS increasing the filling level of the Dirac cone and reducing the filling level of the DS. When the DS is completely emptied due to its finite amount of charge, the new filling level of the TSS positioned above the DP corresponds to the CNL of the combined DS/TSS system. As a result, the DS becomes positively charged and the TSS negatively charged, but in total neutrality condition is fulfilled. For a DS positioned below the VB, as depicted in Fig. 3(b), the charge transfer occurs in the reverse direction. Electrons from the TSS flow into the DS until it is completely filled, which results in a negative DS and a positive TSS with a CNL below the DP for achieving neutrality. In both depicted cases, the filling level of the DS is either completely depleted or completely filled by the charge transfer from or to the TSS, respectively, due to the finite amount of charge inside the DS. However, dependent on the character of the

DS, i.e. position E_{DS} and width, it is also possible that the DS remains partially filled after charge transfer. So in the end, the position of the CNL of the TSS is directly influenced by the presence of additional trivial DS. Both a change of the amount of charge inside the DS or a shift of the position of the DS due to additional surface doping lead directly to a corresponding shift of the CNL describing the complete system composed out of the trivial DS and the TSS. In turn, this CNL value is the starting point for the process of charge transfer with the TI bulk. When the (isolated) TSS/DS system is 'combined' with the TI bulk material, the position of the CNL inside the Dirac cone of the TSS has a strong influence on the amount of charge transfer occurring between the TSS/DS and the bulk material, and, therefore, influences the resulting shape of the near-surface band-bending.

In contrast to the CNL, i.e. the initial filling level of the TSS, which is rather a theoretical quantity describing a neutral TSS/DS system being isolated from the bulk of the crystal and so not measurable, the final filling level of the Dirac cone corresponds to the surface Fermi energy E_F^{top} , which can be directly observed by ARPES measurements. The third important parameter for the charge transfer is the position of the bulk Fermi energy E_F^{bulk} representing the bulk dopant concentration. For an extended bulk crystal, all three parameters, i.e. the CNL, the surface Fermi energy E_F^{top} and the bulk Fermi energy E_F^{bulk} , control the charge transfer inside the TI material, and determine the total charge in the TSS and space charge layer, and thus the corresponding shape of band bending. Due to the overall condition of charge neutrality of the complete TI bulk crystal, the three parameters are dependent on each other. If two values are given, the third value is fixed to fulfill the neutrality condition. So, only E_F^{top} and E_F^{bulk} have to be known for the band

bending simulation and the non-accessible CNL can be calculated with the shape of the Dirac cone known from ARPES as input.

In order to visualize the interplay of the three parameters and their impact on the shape of the band bending in TI bulk crystals, Fig. 4 outlines the band diagrams for three different bulk dopant concentrations, i.e. p-doped (Fig. 4(a)), intrinsic (Fig. 4(b)) and n-doped (Fig. 4(c)). For the calculated diagrams, specific values for either E_F^{top} (blue diagrams) or CNL (gray diagrams) are used, while the respective other value results from the condition of charge neutrality. The relative position of the Fermi energy (dashed line) with respect to the valence band edge at the surface and inside the bulk is described by E_F^{top} and E_F^{bulk} , respectively. For all three blue diagrams in Fig. 4(a)-(c), the value of E_F^{top} is fixed to the midgap position. Such a situation was also experimentally realized for instance for a quaternary BiSbTeSe system [37].

For the p-doped bulk in Fig. 4(a), a downward band bending with a negatively charged space charge region is obtained. So, the TSS is positively charged, which is in agreement with the calculated CNL positioned above E_F^{top} indicating that the filling state of the Dirac cone has been reduced and negative charge has flown into the space charge region (highlighted blue area). For a stronger downward band bending, e.g. as obtained by a degenerately doped bulk, a non-topological 2-dimensional electron gas (2DEG) with quantized states would arise near the surface, as also seen experimentally [38–40], so that a description by Poisson’s equation has to be replaced by the Schrödinger-Poisson approach even for an extended bulk crystal.

In Fig. 4(b), the value of the bulk Fermi energy E_F^{bulk} is changed to midgap position representing the intrinsic character of the bulk and resulting in flat bands (blue lines) due to the assumed midgap position of E_F^{top} . In this case the CNL is equal to E_F^{top} indicating that no charge transfer has occurred. Nevertheless, the value for CNL differs from the value obtained in (a), as it depends directly on E_F^{bulk} in the case of a constant midgap E_F^{top} .

For the n-doped case shown in Fig. 4(c), an upward band bending is obtained with a midgap value of E_F^{top} (blue lines). The calculated CNL is now far below the surface Fermi energy indicating a charge transfer of electrons from the bulk into the Dirac cone.

If now alternatively the value of the CNL is assumed to be constant instead of E_F^{top} , the resulting band bending for the same amount of bulk dopants can be completely different, as it is visualized by the gray colored band diagrams in Fig. 4(b)-(c). Here, such a constant value for the CNL corresponds to a fixed surface configuration with a specific concentration of surface defects or adsorbates. In Fig. 4(b), the flat band condition for the midgap value for E_F^{bulk} vanishes, and instead an upward

band bending is obtained, as now E_F^{top} being dependent on both E_F^{bulk} and CNL is not positioned midgap any more. In Fig. 4(c), with the same position of the CNL than for the gray case in (b), the obtained upward band bending is much weaker and the resulting position of E_F^{top} is different (dashed gray line). Both depicted cases for band bending show that for a specific CNL value the bulk dopant concentration directly influences the value of the surface Fermi energy E_F^{top} . On the other hand, this implies that a variation of the CNL value due to surface doping directly influences the surface Fermi energy, if the bulk dopant concentration remains constant. So, if the surface defect concentration is increased with time, a shifting value of E_F^{top} can be observed by consecutive ARPES measurements. Such effects of surface degradation in TIs due to long-time storage in vacuum or exposure to air have also been observed experimentally [38, 41, 42].

In contrast, if the value for E_F^{top} is constant, the positions of the CNL are all different for different amounts of bulk dopants, as visualized by the blue band diagrams in Fig. 4(a)-(c). In this case, (a)-(c) correspond to different surface configurations, and thus different CNL, but the final result, i.e. the position of the surface Fermi energy E_F^{top} , as measured by ARPES, is the same. So, the knowledge of the position of the CNL is not needed in order to calculate the band diagram. Therefore, it can be concluded that for the case of an extended semi-infinite bulk crystal both the surface Fermi energy E_F^{top} and the bulk dopant concentration represented by E_F^{bulk} have to be known to perform an exact calculation of the near-surface band bending. This is different for TI thin films, for which the band bending can be calculated reasonably well without the knowledge of E_F^{bulk} , as it will be shown in the next section.

B. Thin film: symmetric band bending

In the case of a TI thin film, there exist two TSS on top and bottom surface. However, for thin films grown on a substrate, the bottom TSS is not directly accessible by surface sensitive methods and difficult to investigate. So, if no further information is available, it is a reasonable first approximation to assume that the properties, in particular the filling state, of the bottom TSS is equal to the top TSS. This leads to the symmetric case, in which only information about the top TSS is necessary and the boundary conditions on top and bottom surface are the same. So, if a thin film of thickness d with two interfaces and equal surface Fermi level positions on top and bottom interface is assumed, the problem is symmetric with respect to $z_0 = d/2$ and the appropriate boundary conditions are $\frac{dv}{dz} = 0$ for $z_0 = d/2$ and $v(0) = v(d) = v_{\text{top}} = (E_F^{\text{top}} - E_F^{\text{bulk}})/k_B T$. The solution of Eq. 4 for these boundary conditions leading to a symmetric band-bending can be expressed by

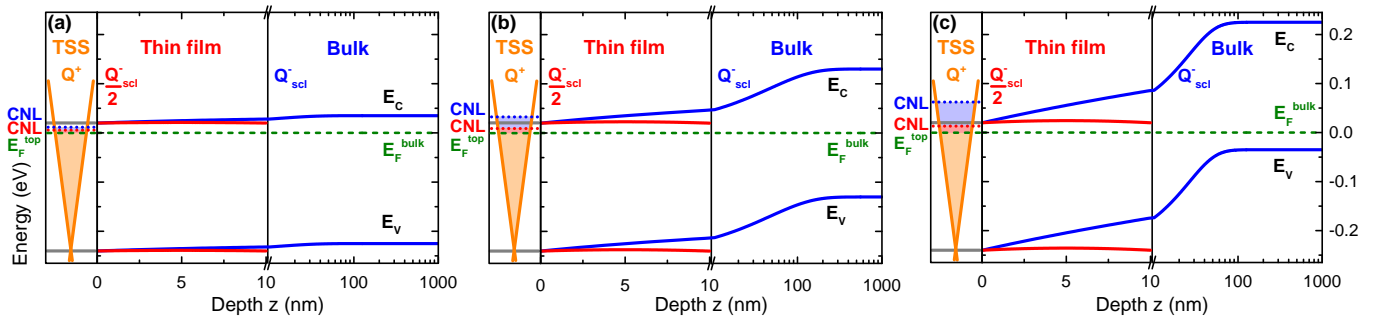


FIG. 5. (Color online) Calculated band diagrams for a 10 nm BiSbTe₃ thin film using the symmetric approximation in dependence of three different film dopant concentrations, i.e. n-doped (a), intrinsic (b) and p-doped (c). For all plots, the value of the surface Fermi energy E_F^{top} is set to 20 meV below the conduction band edge, which results from ARPES measurements [15]. In the middle parts of (a) - (c), the conduction and valence bands of the thin film are shown as function of depth z from the surface (red lines), while in the left parts of (a) - (c) the partially filled Dirac cone (orange lines and area) of the top TSS is depicted. The blue lines indicate the band bending in an corresponding extended bulk crystal exhibiting the same dopant concentration as the thin film. The spacing between the Fermi energy (dashed green line) and the valence band edge inside the bulk of the extended crystal, i.e. E_F^{bulk} , directly represents the dopant character of the bulk material and changes across the band gap for the different dopant levels. In contrast, the band positions in the film are not influenced significantly from (a) to (c) and remain nearly constant. So, the band bending in the thin film is nearly independent of the film dopant concentration because of the long screening length and only governed by the position of E_F^{top} . The CNL (colored dotted lines) are different for a thin film (red) and a bulk crystal (blue) with the same dopant concentration, but are positioned above E_F^{top} indicating a transfer of negative charges from the TSS to the film or bulk.

$$z(v) = \text{sgn}(-v) \frac{L}{\sqrt{2}} \int_{v_{\text{top}}}^{v(z)} \sqrt{\frac{e^{u_b} + e^{-u_b}}{e^{u_b} \left(e^v - e^{v(\frac{d}{2})} - v + v(\frac{d}{2}) \right) + e^{-u_b} \left(e^{-v} - e^{-v(\frac{d}{2})} + v - v(\frac{d}{2}) \right)}}} dv, \text{ for } 0 \leq z \leq \frac{d}{2} \quad (7)$$

which has to be calculated iteratively, as the constant value for v ($z = \frac{d}{2}$) is not known. So, in the first iteration step the value for v ($z = \frac{d}{2}$) is determined by numerical inversion and then the equation is solved for the remaining values $v(z)$ in the interval $0 \leq z < \frac{d}{2}$. This case of band bending in a thin film has been considered before in the simplified approach of the Schottky approximation [43, 44]. However, the Schottky approximation is only valid for depletion layers with a strong band bending $|eV_{\text{top}}| \gg k_B T$, where all free charge carriers flow from the film material into the TSS resulting in a completely depleted and insulating film. But as the direction and amount of charge transfer is determined by multiple parameters, as shown before in detail, depletion layers with small band bending and also the formation of an accumulation layer are possible, for which a description within the Schottky approximation is not sufficient.

In order to include the quantization arising from the confinement of thin films, subsequently the Schrödinger equation is solved. As an approximation for a weak band-bending, which turns out to occur in the case discussed in the following, the solution for a square potential with infinite barrier height is used. Due to the confinement in a square well the occupation of the bands is quantized in one dimension leading to a modified effective

density of states, which is taken into account in the next iteration, i.e. the subsequent solution of Poisson's equation. Further details of the calculation can be found in the supplemental material [32]. It turns out that the results for the calculated mobile charge carrier density inside the TI thin film discussed in the following are reduced in the Schrödinger-Poisson approach by a factor of (2 - 2.5) compared to the pure classical approach, i.e. solving Poisson's equation.

In the thin-film limit, the shape of the near-surface band-bending is determined by the value of the surface Fermi energy E_F^{top} , the position of the CNL in the TSS and the dopant concentration of the TI film, as it also applies for the case of a semi-infinite bulk crystal. However, an additional parameter is now the thickness of the thin film, as this quantity influences the amount of charge, which can be transferred between TSS and TI film. For a decreasing thickness, the amount of charge in the space charge region of the thin film also decreases, if the other three parameters remain constant. As a result of this reduced amount of charge, the band bending becomes increasingly weaker, as the boundary conditions on both surfaces still have to be satisfied. Again, all four parameters are dependent on each other, so that one parameter is given by the other three. However, it turns out that

a significant difference compared to the case of the semi-infinite bulk crystal is, that for a 10 nm thin film the band bending inside the film is largely independent of the dopant concentration of the film and remains rather fixed to the surface position for a varying dopant level. So, the position of the Fermi energy inside the film deviates strongly from the bulk Fermi energy E_F^{bulk} of a corresponding semi-infinite bulk crystal with the same dopant concentration.

In order to visualize this different behavior by means of an example, in Fig. 5 the calculated band-bending for the TI system BiSbTe₃ is plotted as function of depth z into the sample for three different bulk dopant concentrations, i.e. n-doped (Fig. 5(a)), intrinsic (Fig. 5(b)) and p-doped (Fig. 5(c)). The red band diagrams correspond to a 10 nm thin film and the blue lines describe a corresponding extended bulk crystal with the same dopant concentration and position of surface Fermi energy E_F^{top} as in the case of the thin film. For the calculation, a band-gap of 260 meV and a surface Fermi energy of $E_F^{\text{top}} = 240$ meV above the valence band edge are used, whereby the position of the Dirac point coincides with the edge of the valence band, and the effective mass is set to a value of $m^* = 0.15 m_e$, as it has been measured by ARPES [15]. As the film thickness influences the charge transfer and thus the band bending, the CNL for thin film (red dotted line) and bulk crystal (blue dotted line) have to be different, if the value for E_F^{top} determined by ARPES is fixed and only the dopant concentration is varied. This general behavior is depicted in Fig. 5(a) to 5(c) for the cases from an n-doped to a p-doped material. For the bulk crystal (blue curves), the variation of dopants strongly influences the relative position between the Fermi energy and the valence band edge, represented by the value of the bulk Fermi energy E_F^{bulk} , and results in a strong increase of the near-surface band-bending from p-type to n-type dopants. However, in the thin-film limit, the bending of the bands remains very weak for all cases of dopant types and is largely independent on the dopant concentration. The relative spacing of the Fermi energy and the valence band edge inside the thin film is not significantly influenced by a shift of the film dopant concentration and remains close the value at the surface. Thus, the valence band position can differ strongly from its value of a corresponding bulk crystal with the same amount of dopants, as it is visible in Fig. 5(c).

Such an observed weak band-bending in a thin film can be explained by the long screening length compared to the small film thickness. If the screening length is much larger than half of the film thickness, the amount of charges inside the film material is not sufficient to establish a similar space charge region as for the case of an extended bulk crystal. The charge transfer between TSS and film material occurs until an equilibrium condition is achieved, but as the amount of mobile charges in the film is limited due to a small number of donors/acceptors, such a small charge exchange between TSS and film ma-

terial leads only to a weak band bending. At this point, it is important to distinguish between dopant and doping concentration, as the first one describes the amount of defects in the material, e.g. given by growth conditions, and the second one corresponds to the amount of mobile charge carriers in the material. Inside an extended crystal, it is expected that the amount of dopants directly influences the doping, but for a thin film with an additional source of charges (TSS) this is not necessarily true. For example, the dopant concentration in the film shown in Fig. 5 corresponds to an intrinsic bulk material. In the case of the depicted downward band-bending, the amount of electrons transferred from the TSS to the film material (red area in the Dirac cone) is much lower than in the case of the extended bulk crystal (blue area). Nevertheless, the transferred charges from the TSS are sufficient to nearly fully dope the film in an *n*-type way (Fig. 5(b)), or even completely saturate all acceptors in the film material (Fig. 5(c)) and resulting in the same *n*-doping as in (b). As there is a small increase in charge transfer from (a) to (c), also the band bending increases slightly, but it is still very weak compared to the bulk case (blue). The weak band-bending can also be explained mathematically using Eq. (3) describing the curvature of the band bending. As it is limited to a maximum value and as also the boundary conditions for the bands on top and bottom surface of the film have to be fulfilled, only a weak bending is obtained on the length scale of a thin film. On the other hand, if the film thickness approaches the screening length, the charge transfer between TSS and film increases resulting in an increasingly stronger band bending, and if the thickness exceeds twice the screening length, the established space charge region is the same as in an extended bulk crystal.

As the width of the space-charge region scales with the Debye length, a long screening length can be caused, besides a low dopant concentration also by e.g. a high value of the dielectric constant. For example, for the material BiSbTe₃ a value of $\epsilon \approx 100$ is reported [12–14]. Thus, for the case of such a high ϵ material, the screening length easily exceeds the thickness of ultra thin films. So, the positions of the bands across the thin film do not deviate significantly from their positions at the surface defined by the value of E_F^{top} and are nearly independent of the film dopant concentration. In turn, this enables to approximate the total mobile charge carrier concentration in the thin film from information gained by surface-sensitive measurements, even if the exact dopant concentration inside the film material remains unknown.

In Fig. 5(a)-(c), only a downward bending of the bands is depicted because the surface Fermi energy is positioned very close to the conduction band. Nevertheless, also an upward band-bending is possible for a larger amount of *n*-type dopants in the bulk material. In this case the doping level would become degenerate with a bulk Fermi energy positioned inside the conduction band. However, the effect on a thin film would be the same as for the case of downward band bending, and only the direction of charge

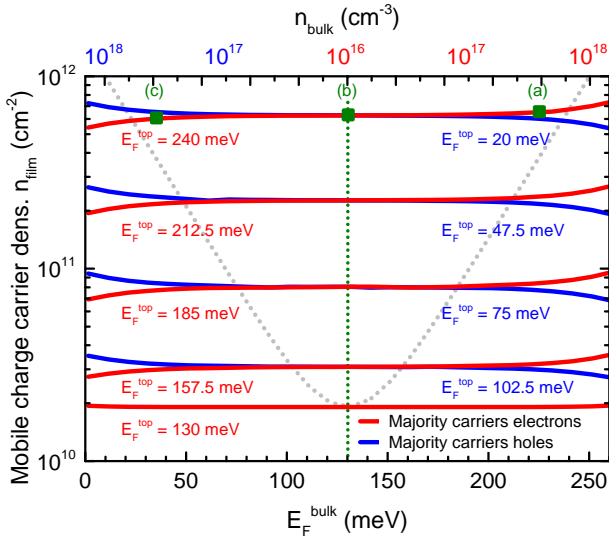


FIG. 6. (Color online) Integrated total mobile charge carrier density n_{film} inside the thin film using the symmetric approximation as function of the dopant concentration represented by the value of the bulk Fermi energy E_F^{bulk} . The value of the surface Fermi energy E_F^{top} is an additional free parameter. On the upper horizontal axis, the associated 3D charge carrier density of the bulk crystal n_{bulk} is shown. Inside the band-gap the calculated film carrier density is approximately constant and, thus, independent of the dopant concentration. The red and blue lines indicate the type of majority carriers in the thin film formed by electrons and holes, respectively. The three green squares correspond to the values of E_F^{bulk} used in the band diagrams in Fig. 5(a)-(c), while the dotted green line corresponds to a cut shown in the plot in Fig. 8. For comparison, the dotted gray line shows the strong exponential dependency of the charge carrier density expected for an extended bulk crystal for the case of $E_F^{\text{top}} = 240$ meV (values converted in 2D units for a 10 nm thin film).

transfer between TSS and film reverses. Electrons from the film flow into the TSS, so that due to the limited amount of charge the Fermi energy inside the film drops below the conduction band and in the end nearly coincides with the position at the surface of the film resulting in a weak upward band bending. Only for a very strong degenerate doping, the screening length can become so small, that a stronger band bending is obtained in the thin film. However, such a high dopant concentration of the bulk would be in contradiction with the aim of tailored film growth of ternary TI material systems, which should result in a minimization of the bulk material conductivity and, thus, in a Fermi energy positioned inside the band gap [16]. For this reason, we exclude the case of upward band bending for the material BiSbTe₃ discussed here. Furthermore, for the degenerately doped case, the Boltzmann approximation can not be used any more and all calculations have to be done by using the Fermi distribution. Indeed, such an extension of the calculations is possible, but the equations would become much more complicated. Already a value of E_F^{top} positioned 20 meV

below the conduction band edge is very close to the limit of the Boltzmann approximation. In this case, the error is up to 50 %, but as the Boltzmann distribution becomes larger compared to the Fermi distribution, the calculated band bending is only overestimated and might be effectively less than the already obtained weak bending.

For a different value of E_F^{top} positioned not so close to the conduction band, an upward band bending can be present. Within the Schottky approximation such an upward band bending in TI systems and thin films has been discussed recently [43, 44]. For a value of the surface Fermi energy located closer to mid-gap, as it is the case in some experiments [45, 46], and appropriate values for the film thickness and screening length, a TI thin film can get nearly fully depleted, as almost all negative mobile charge carriers flow into the TSS. This would result also in a near-midgap position of the Fermi energy inside the film and so almost in a completely insulating film material. However, this can be excluded for the special case of BiSbTe₃ with $x = 0.5$ discussed here, as the position of E_F^{top} is very close to the conduction band edge, as measured by ARPES [15, 47].

As long as E_F^{top} is positioned below the conduction band edge, also a strong downward band-bending can be excluded, which would produce a non-topological 2DEG near the surface. Such a 2DEG has been observed in recent studies [38–40], but in all these cases the surface Fermi energy is positioned deep inside the conduction band at the surface of the film, while the Fermi energy inside the film material is still inside the band gap, which is not the case for the discussed BiSbTe₃.

The assumption of the same E_F^{top} in Fig. 5 (a)-(c) corresponds to a value measured by ARPES. The different values for the CNL indicate that the surface doping concentration due to adsorbates or surface defects is different for the cases depicted in (a) to (c), so that all band diagrams correspond to sample systems with different concentrations of surface defects. Within this perspective, all depicted band diagrams are possible initial states, which result in the final state observed by a particular ARPES measurement (i.e. $E_F^{\text{top}} = 240$ meV). The different CNL positions indicate the different amount of charge transfer between TSS and film or bulk, respectively. On the contrary, if the value for the CNL is kept constant in experiment corresponding to specific density of surface defects, a variation of the dopant concentration in the film would directly lead to a different position of E_F^{top} , which could be seen in ARPES. Additional band diagrams visualizing such cases of constant CNL can be found in the Supplementary Material [32].

Within the Boltzmann approximation, the mobile charge carrier density can be calculated from the potential $v(z)$ by $n_e(z) = n_b \exp[v(z)]$ and $p_h(z) = p_b \exp[-v(z)]$ for electrons and holes, respectively. Integrating $n_e(z)$ and $p_h(z)$ over the thickness d of the thin film results in the total mobile charge carrier density n_{film} inside the film material. In general, this quantity is both dependent on the film dopant concentration, which

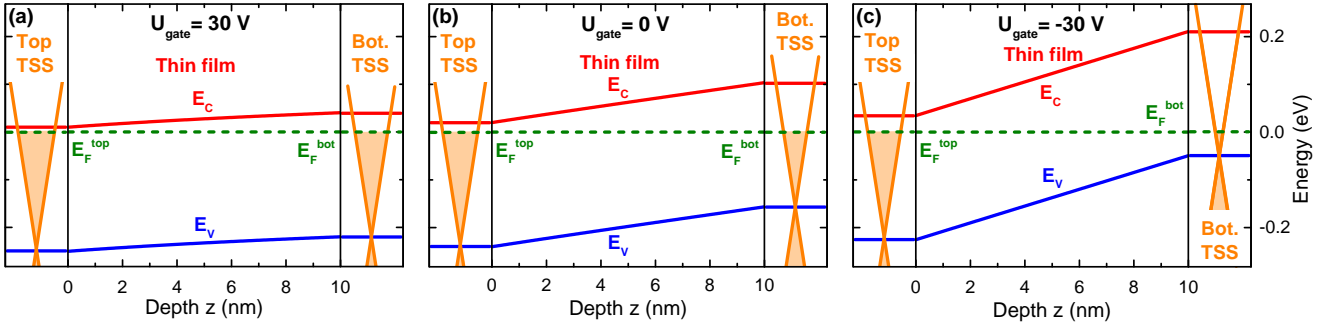


FIG. 7. (Color online) Gate-dependent band-bending for a 10 nm thin BiSbTe₃ film with intrinsic dopant concentration ($E_F^{\text{bulk}} = 130$ meV) as function of the depth z into the film for different gate voltages, i.e. 30 V (a), 0 V (b) and -30 V (c). The calculation is based on the asymmetric approach with the same parameters as used in Fig. 5 and additional information from gate-dependent transport measurements [15]. Due to different values of the surface Fermi energies E_F^{top} at $z = 0$ and E_F^{bot} at $z = 10$ nm, the resulting band bending in the thin film is asymmetric. The top surface value E_F^{top} can be measured directly by ARPES, while the bottom value E_F^{bot} can be extracted by gate-dependent transport measurements [15]. The application of a bottom gate electrode influences both surface Fermi levels in a different way and leads to an increase in the strength of band bending from (a) to (c) as function of gate voltage, as described in detail in [15]. Thus, the mobile charge carrier density inside the thin film is significantly influenced by the gate voltage.

is represented in the equations by the bulk Fermi energy E_F^{bulk} of a corresponding bulk crystal with same dopant density, and on the value for the surface Fermi energy E_F^{top} , as expressed by

$$n_{\text{film}}(E_F^{\text{top}}, E_F^{\text{bulk}}) = \int_0^d n_i \left(e^{[u_b(E_F^{\text{bulk}}) + v(z, E_F^{\text{top}}, E_F^{\text{bulk}})]} + e^{-[u_b(E_F^{\text{bulk}}) + v(z, E_F^{\text{top}}, E_F^{\text{bulk}})]} \right) dz \quad (8)$$

with n_i denoting the intrinsic charge carrier concentration. In Fig. 6, the total mobile charge carrier density is plotted for a 10 nm thin film BiSbTe₃ [15] as function of the dopant level expressed by the bulk Fermi energy E_F^{bulk} . The value of the surface Fermi energy E_F^{top} is an additional free parameter. Within the band-gap, the charge carrier concentration inside the thin film is nearly independent of the value for the bulk Fermi level and, thus, the dopant level of the film, as indicated by the approximately horizontal lines. Only in the vicinity of the band edges, where also the Boltzmann approximation becomes less applicable, a deviation from the constant behavior is visible. However, across the majority of the band gap, the absolute value of the carrier concentration is only influenced by the position of the surface Fermi energy E_F^{top} and not by the dopant concentration in the film, so that $n_{\text{film}}(E_F^{\text{top}}, E_F^{\text{bulk}}) \approx n_{\text{film}}(E_F^{\text{top}})$. Thus, by measuring the surface Fermi energy, the amount of charge carriers inside the TI thin film can be determined, even if the dopant concentration (E_F^{bulk}) is unknown, and if also the mobility of the material is known, the conductivity of the film interior conduction channel in the TI system can directly be calculated. This is in strong contrast to the behavior for an extended bulk crystal, where the charge carrier density shows a strong dependence on the

dopant concentration, which is visualized by the dotted gray curve in Fig. 6.

As a quantitative example, for a surface Fermi energy of 240 meV, as determined in [15], the calculated charge carrier concentration inside the BiSbTe₃ film using the symmetric approximation is $\sim 6 \cdot 10^{11} \text{ cm}^{-2}$, which is close to the charge carrier density inside the Dirac cone of the top TSS of $4 \cdot 10^{12} \text{ cm}^{-2}$, indicating that there might be a contribution to charge transport in the TI system by the bulk channel. In this case, it turns out that the mobility of the bulk material at room temperature is very low ($< 2 \text{ cm}^2/\text{Vs}$) compared to the TSS channels, so that the conductivity of the bulk channel is negligible for the overall current transport. However, this can be completely different for other material systems, especially at low temperatures, where the mobility can be larger by a factor of 10 - 50, so that each individual case has to be considered.

C. Thin film: asymmetric band bending

The previously discussed symmetric case is a simplified approximation of the band-bending in the TI thin film. As only the position of the top surface Fermi level is directly accessible by measurements (ARPES), the bottom surface Fermi energy is assumed to be the same. However, this might not be completely true, as a different environment and thus surface defect density of the bottom TSS results in different top and bottom surface Fermi energies. So, in general, the boundary conditions on both interfaces of the TI thin film are not symmetric, as the positions of the Fermi levels E_F^{top} and E_F^{bot} can be different. For such an asymmetric band-bending in a thin film, the calculation is more complex and considered in detail in the appendix.

In order to calculate the band-bending in a thin film by using the asymmetric approach, both values for the top and bottom surface Fermi level E_F^{top} and E_F^{bot} have to be known. The top surface Fermi energy can be directly measured by ARPES, while the bottom value can be extracted from gate-dependent four-point transport measurements, as it is described in detail in [15]. In this case, a bottom gate electrode is applied to the TI thin film and the four-point resistance of the TI film is measured by a multi-tip STM as function of the applied gate voltage. Due to quantum capacitance effects arising from

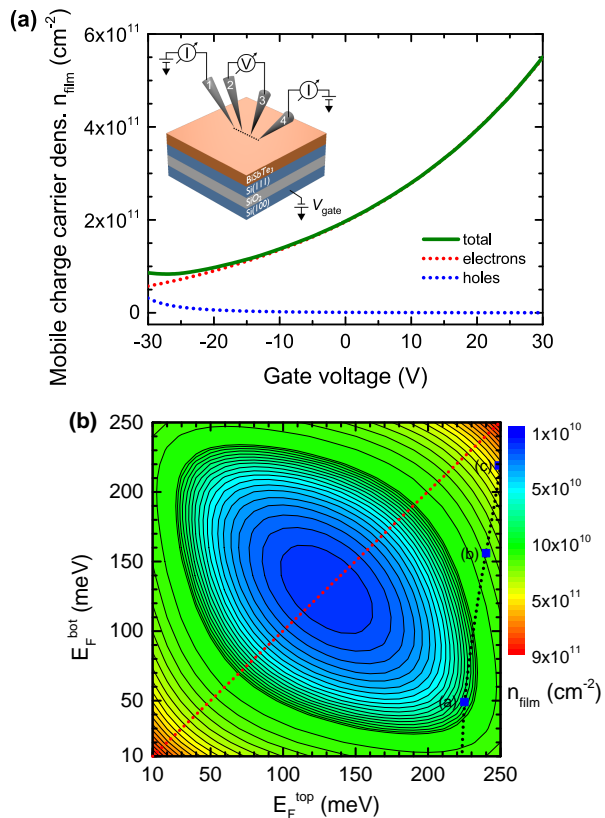


FIG. 8. (Color online) (a) Calculated mobile charge carrier density n_{film} inside a 10 nm thin film BiSbTe₃ as function of the applied gate-voltage (solid green line). The calculation is based on the asymmetric approach for the band-bending inside the film and on parameters from [15]. The individual contributions by electrons (red) and holes (blue) are depicted by the dotted lines. In the inset, the measurement setup and the sample configuration is shown [15]. (b) Color plot of the mobile charge carrier density n_{film} as function of the top and bottom surface Fermi energy E_F^{top} and E_F^{bot} , respectively, for the specific case considered in [15]. The charge carrier density is calculated for a thin film with intrinsic dopant concentration. The diagonal dotted red line indicates the symmetric case with $E_F^{\text{top}} = E_F^{\text{bot}}$ and corresponds to a cut at the position of the dotted green line in Fig. 6. The marked blue points correspond to the charge carrier concentrations resulting from the band diagrams depicted in Fig. 7(a)-(c), while the dotted black line in between shows the general gate-dependent behavior.

the small DOS in the TSS, the induced charge carriers on the bottom gating electrode do not only have a strong influence on the filling state of the bottom TSS Dirac cone, but also on the amount of charges in the top TSS. So, if the top value of the Fermi energy E_F^{top} is known, the bottom value E_F^{bot} can be determined by using gate dependent measurements, as described in [15].

In order to include quantization effects in the asymmetric case, a triangular well of length d limited by barriers of infinite height on both sides is considered. The slope of the triangular well is determined by the difference between the top and bottom surface Fermi levels E_F^{top} and E_F^{bot} . Such an approach with a triangular shape without a curvature can be used as approximation because of the weak band bending. Further details of the calculations are shown in the supplemental material [32].

As an example, in Fig. 7(a)-(c), the asymmetric band bending in a 10 nm BiSbTe₃ TI thin film is shown for three different gate voltages, i.e. 30 V (7(a)), 0 V (7(b)) and -30 V (7(c)). All three band diagrams are calculated for an intrinsic film dopant concentration ($E_F^{\text{bulk}} = 130$ meV), but also for a different amount of dopants the band-bending in the film-limit is approximately the same, as it has been shown in the previous section. The varying gate voltage causes a different amount of induced charge carriers in the top and bottom TSS [15], and thus results in different filling levels of the Dirac cones and different values for the surface Fermi energies E_F^{top} and E_F^{bot} , respectively, which are shown in Fig. 7(a)-(c). The strength of the band-bending increases with negatively increasing gate voltage (Fig. 7(a)-(c)), as the charge carriers in the bottom TSS are stronger influenced by the gating than in the top TSS. As a result, also the charge carrier density inside the thin film varies strongly for different gate voltages. However, if only a fixed value for the gate voltage is considered, but the dopant concentration of the film is changed, the integrated charge carrier density remains nearly constant. So, if the strongly z-dependent carrier density is integrated over the thin film and plotted as function of the film dopant concentration, represented by the bulk Fermi energy of a corresponding extended crystal, nearly the same dependency results, as it has been shown previously in Fig. 6 for the symmetric approximation. A plot of this gate-dependent integrated charge carrier density as function of E_F^{bulk} can be found in the supplementary material [32]. Thus, also in this case the absolute value of the total mobile charge carrier density n_{film} inside the thin film does not depend on the amount of dopants or correspondingly on E_F^{bulk} due to the same reasons as discussed before for the symmetric approximation. As a result, the total charge carrier density and the resulting conductivity of the interior of a TI thin film only depends on the applied gate voltage. This dependency is plotted for the case of 10 nm BiSbTe₃ in Fig. 8(a), where the total mobile carrier density (green line) and the contributions due to electrons (dotted red line) and holes (dotted blue line) are shown. The inset depicts the measurement setup used in [15].

If the asymmetric approach is compared to the more simplified symmetric approximation discussed before, it is reasonable that there are differences in the calculated values depending on the input parameters. For a given parameter set of E_F^{top} and E_F^{bot} the value for the mobile charge carrier density in a thin film n_{film} can differ from the calculated value using only the symmetric approximation. The deviation between both values depends mainly on the difference between E_F^{top} and E_F^{bot} . This is visualized in Fig. 8(b) with a color plot of the total mobile charge carrier density inside a 10 nm BiSbTe₃ thin film (based on parameters from [15]) as function of the top and bottom surface Fermi levels. The diagonal dotted red line corresponds to the symmetric case with $E_F^{\text{top}} = E_F^{\text{bot}}$. For deviations from this equality, e.g. along the vertical axis caused by a unknown E_F^{bot} , while the measurable value for E_F^{top} is fixed, the charge carrier concentration can deviate up to one order of magnitude. Overall, the contour lines are symmetric due to the contributions of electron and holes to the total mobile charge carrier density. The blue points correspond to the charge carrier densities obtained for the gate-dependent band diagrams depicted in Fig. 7(a)-(c), while the dotted connection line between the points expresses the general gate-dependency of n_{film} shown in Fig. 8(a) as function of E_F^{top} and E_F^{bot} . For example, for values for the top and bottom surface Fermi level of 240 meV and 156 meV, respectively, as determined in [15] for a vanishing gate voltage, the calculated charge carrier density inside the film is $\sim 2 \cdot 10^{11} \text{ cm}^{-2}$, which is only one third of the value calculated by using the symmetric approximation. So, the charge carrier density inside the TI thin film material can be calculated more precisely using the asymmetric model due to the inclusion of additional information for the bottom surface. As the gate-dependent measurements can provide the mobility of the film, finally the conductivity of the interior of the TI film can be determined [15].

IV. CONCLUSION

In conclusion, we have shown that topological insulator thin films can exhibit parallel parasitic conduction channels through the interface layer and interior material of the film, which can participate in current transport and therefore significantly reduce the amount of current flowing through the TSS channel, so that the desired beneficial properties of the TI, like e.g. spin-momentum locking, would be partially lost. If the parasitic conductance channels are understood in detail, this opens the possibility to tune them towards a negligible influence compared to the auspicious TSS conductance channel.

In order to determine the interface conductivity of TI thin films grown by van-der-Waals epitaxy, only the initial substrate termination has to be prepared and, afterwards, the interface conductivity can directly be measured by surface-sensitive four-probe transport measurements performed with a multi-tip STM, as it was demon-

strated using the example of the Te/Si(111)-(7×7) interface.

The conductivity of the interior of the film can be calculated by a combination of both band-bending calculations using the thin-film limit and surface-sensitive experimental methods, such as ARPES and gate-dependent four-probe transport measurements. By using the symmetric approximation, which applies the measured value of the top surface Fermi level (ARPES) also to the non-accessible bottom surface, the total mobile charge carrier density inside the film material can be calculated, even if the amount of dopants unintentionally incorporated during film growth is unknown, as in the thin-film limit the carrier density is nearly independent of the film dopant concentration.

The calculations can be refined by the asymmetric approach using additionally gate-dependent four-probe measurements on the top surface as input. Using this approach, the conductivity of the interior of the thin film can be calculated and the role of this channel for current transport in the TI system can be classified.

Overall, the presented methods are general and can be applied to very different TI material classes. The information gained from this methods are important for designing future electronic devices based on TI materials in a way that the majority of current is exclusively transported by the TSS channel and the most benefit can be taken from the TI properties.

Appendix: asymmetric band-bending

In the following, the equations for the calculation of the band-bending in the framework of the asymmetric approach based on the solution of Eq. (4) are presented in detail. Concerning the boundary conditions, three different cases (A) - (C) can be distinguished, which are shown schematically in Fig. 9: (A) $\frac{dv}{dz} \Big|_{z=z_0} = 0$ for $0 \leq z_0 \leq d$, (B) $\frac{dv}{dz} \Big|_{z=z_0} \neq 0$ for $0 \leq z_0 \leq d$, and (C) $v(z = z_0) = 0$ for $0 \leq z_0 \leq d$. For the cases (A) and (B) the signs of the surface potentials v_{top} and v_{bot} are equal, and for the case (C) the signs are different. In order to simplify the calculation of the band-bending for the cases (A) and (C) the function $v(z)$ can be split into two parts $v_1(z_1)$ for $0 \leq z_1 \leq z_0$ and $v_2(z_2)$ for $0 \leq z_2 \leq d - z_0$, where $z_2 = d - z_1$, as the origin of $v_2(z_2)$ is situated on the bottom surface of the thin film. The transition between v_1 and v_2 at position z_0 should be continuous, leading to the transition conditions for (A) $v_1(z_0) = v_2(d - z_0) := v_0$ and $\frac{dv_1}{dz_1} \Big|_{z_1=z_0} = -\frac{dv_2}{dz_2} \Big|_{z_2=d-z_0} = 0$, and for (C) $v_1(z_0) = v_2(d - z_0) = 0$ and $\frac{dv_1}{dz_1} \Big|_{z_1=z_0} = -\frac{dv_2}{dz_2} \Big|_{z_2=d-z_0}$, respectively. The other two boundary conditions are determined by the initial values of the potential $v_1(0) = v_{\text{top}}$ and $v_2(0) = v_{\text{bot}}$ at the surfaces of the film. In case (B) only one function, either $v_1(z_1)$ or $v_2(z_2)$, has to be calculated and the two boundary conditions are $v_{1,2}(0) = v_{\text{top}}$ and $v_{1,2}(d) = v_{\text{bot}}$. In detail, the results for the band-

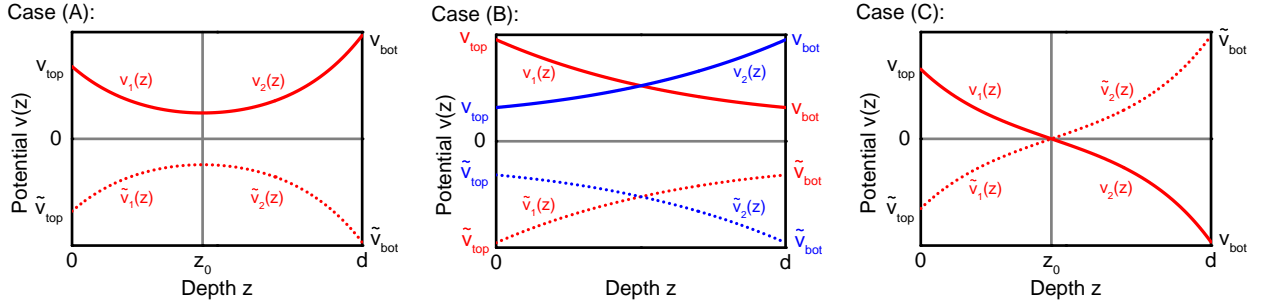


FIG. 9. (Color online) (a)-(c) Three different cases (A) - (C) for the asymmetric band-bending $v(z)$ with different surface potentials v_{top} and v_{bot} on the two interfaces of a thin film with thickness d . The dotted lines correspond to the results from boundary conditions with inverted signs compared to the boundary conditions for the solid lines. In (b), the blue line indicates the result for interchanging the values of v_{top} and v_{bot} compared to the red line.

bending $v_i(z_i)$ for the cases (A) - (C) obtained by inserting the appropriate boundary conditions in Eq. 4 are listed in the following. Hereby, the index $i = 1, 2$ indicates the two parts $v_1(z_1)$ and $v_2(z_2)$, respectively, and $v_{\text{top}, \text{bot}}$ represents the corresponding surface potential, i.e. for $i = 1$ the first index (v_{top}) and for $i = 2$ the second index (v_{bot}) has to be used.

1. Case (A)

In Fig. 9a, the band-bending corresponding to case (A) is shown (red lines). The values of the surface potential v_{top} and v_{bot} are either both positive (solid line) or negative (dotted line), and exhibit only a small difference. Due to the resulting local minimum (maximum), the potential can be separated into two parts v_1 and v_2 . Both can be calculated by the equation

$$z_i(v_i) = \text{sgn}(-v_i) \frac{L}{\sqrt{2}} \int_{v_{\text{top}, \text{bot}}}^{v_i(z_i)} \underbrace{\sqrt{\frac{e^{u_b} + e^{-u_b}}{e^{u_b}(e^{v_i} - e^{v_0} - v_i + v_0) + e^{-u_b}(e^{-v_i} - e^{-v_0} + v_i - v_0)}}}_{:=F_A(u_b, v_i, v_0)} dv_i \quad (\text{A.1})$$

for $0 \leq z_1 \leq z_0$ and $0 \leq z_2 \leq d - z_0$, respectively, with the auxiliary condition determining the constant v_0

$$\text{sgn}(-v_{\text{top}}) \frac{L}{\sqrt{2}} \left[\int_{v_{\text{top}}}^{v_0} F_A(u_b, v_1, v_0) dv_1 + \int_{v_{\text{bot}}}^{v_0} F_A(u_b, v_2, v_0) dv_2 \right] - d = 0. \quad (\text{A.2})$$

2. Case (B)

Fig. 9(b) depicts the case (B), where the local minimum (maximum) in the potential has vanished due to a larger difference between the boundary values resulting in a more pronounced band bending. This case is applied for the calculation of the gate dependent band-bending in section (C) of the main text. Again, the values for v_{top} and v_{bot} have both the same sign (solid and dotted lines), and for exchanged contrary values of v_{top} and v_{bot} (red and blue lines) either v_1 or v_2 has to be determined. Both

potential functions can be calculated by the equation

$$z_i(v_i) = \text{sgn}(-v_i) \frac{L}{\sqrt{2}} \times \int_{v_{\text{top}, \text{bot}}}^{v_i(z_i)} \underbrace{\sqrt{\frac{e^{u_b} + e^{-u_b}}{e^{u_b}(e^{v_i} - v_i + c) + e^{-u_b}(e^{-v_i} + v_i + c)}}}_{:=F_B(u_b, v_i, c)} dv_i \quad (\text{A.3})$$

for $0 \leq z_1 \leq d \Leftrightarrow |v_{\text{top}}| > |v_{\text{bot}}|$ or for $0 \leq z_2 \leq d \Leftrightarrow |v_{\text{top}}| < |v_{\text{bot}}|$, respectively, with the auxiliary condition determining the constant c according to the equation

$$B \int_{v_{\text{top}}}^{v_{\text{bot}}} F_B(u_b, v_i, c) dv_i - d = 0 \quad (\text{A.4})$$

with the prefactor $B = \text{sgn}(|v_{\text{top}}| - |v_{\text{bot}}|) \text{sgn}(-v_{\text{top}}) \frac{L}{\sqrt{2}}$.

3. Case (C)

In Fig. 9c, the band bending according to case (C) is visualized. As the values for v_{top} and v_{bot} have different signs, there is a root in between at z_0 separating the potential into two parts v_1 and v_2 . In the TI thin film, this corresponds to a change of the type of band bending, i.e. a depletion or accumulation zone. Both parts can be calculated by applying Eq. (A.3) for $0 \leq z_1 \leq z_0$ and $0 \leq z_2 \leq d - z_0$, respectively, with the modified auxiliary condition determining the constant c by

$$\text{sgn}(-v_{\text{top}}) \frac{L}{\sqrt{2}} \int_{v_{\text{top}}}^{v_{\text{bot}}} F_B(u_b, v_1, c) dv_1 - d = 0. \quad (\text{A.5})$$

$$C \int_{v_{\text{top,bot}}}^{v_{\text{top,bot}}-\Delta} \sqrt{\frac{e^{u_b} + e^{-u_b}}{e^{u_b} (e^{v_i} - e^{v_{\text{top,bot}}-\Delta} - v_i + v_{\text{top,bot}} - \Delta) + e^{-u_b} (e^{-v_i} - e^{-v_{\text{top,bot}}+\Delta} + v_i - v_{\text{top,bot}} + \Delta)}}} dv_i = d. \quad (\text{A.6})$$

with the prefactor $C = \text{sgn}(-v_i) \frac{L}{\sqrt{2}}$. If now $||v_{\text{top}}| -$

Besides the previously discussed equations applicable within the cases (A) - (C), the transitions conditions between the different cases are also important. Starting from the symmetric case of band-bending with $v_{\text{top}} = v_{\text{bot}}$ as basis, Case (A) has to be applied, if there is a slight distortion between v_{top} and v_{bot} breaking the symmetry. However, if the local minimum (maximum) of the potential function $v_{1,2}(z_{1,2})$ has reached the interface of the film ($z_{1,2} = d$) due to a larger difference of $|v_{\text{top}}|$ and $|v_{\text{bot}}|$, there is a transition to Case (B). The transition condition is $\frac{dv_{1,2}}{dz_{1,2}}|_{z_{1,2}=d} = 0$ with $v_{1,2}(d) := v_{\text{top,bot}}^* = v_{\text{top,bot}} - \Delta$ so that from equation (6) the difference Δ , beyond which the transition occurs, can be calculated as

$|v_{\text{bot}}| \leq \Delta$, Case (A) is used, and if $||v_{\text{top}}| - |v_{\text{bot}}|| > \Delta$, Case (B) has to be applied. If the signs of v_{top} and v_{bot} become different, Case (C) occurs.

-
- [1] D. Hsieh, Y. Xia, D. Qian, L. Wray, F. Meier, J. H. Dil, J. Osterwalder, L. Patthey, A. V. Fedorov, H. Lin, A. Bansil, D. Grauer, Y. S. Hor, R. J. Cava, and M. Z. Hasan, *Physical Review Letters* **103** (2009), 10.1103/physrevlett.103.146401.
- [2] P. Roushan, J. Seo, C. V. Parker, Y. S. Hor, D. Hsieh, D. Qian, A. Richardella, M. Z. Hasan, R. J. Cava, and A. Yazdani, *Nature* **460**, 1106 (2009).
- [3] H. Zhang, C.-X. Liu, X.-L. Qi, X. Dai, Z. Fang, and S.-C. Zhang, *Nature Physics* **5**, 438 (2009).
- [4] L. Barreto, L. Kühnemund, F. Edler, C. Tegenkamp, J. Mi, M. Bremholm, B. B. Iversen, C. Frydendahl, M. Bianchi, and P. Hofmann, *Nano Letters* **14**, 3755 (2014).
- [5] Z. Ren, A. A. Taskin, S. Sasaki, K. Segawa, and Y. Ando, *Physical Review B* **82** (2010), 10.1103/physrevb.82.241306.
- [6] I. Miccoli, F. Edler, H. Pfür, and C. Tegenkamp, *Journal of Physics: Condensed Matter* **27**, 223201 (2015).
- [7] P. Hofmann and J. W. Wells, *J. Phys.: Condens. Matter* **21**, 013003 (2009).
- [8] C. Durand, X.-G. Zhang, S. M. Hus, C. Ma, M. A. McGuire, Y. Xu, H. Cao, I. Miotkowski, Y. P. Chen, and A.-P. Li, *Nano Lett.* **16**, 2213 (2016).
- [9] S. Just, M. Blab, S. Korte, V. Cherepanov, H. Soltner, and B. Voigtländer, *Physical Review Letters* **115** (2015), 10.1103/physrevlett.115.066801.
- [10] S. Just, H. Soltner, S. Korte, V. Cherepanov, and B. Voigtländer, *Physical Review B* **95** (2017), 10.1103/physrevb.95.075310.
- [11] F. Lüpke, S. Just, G. Bihlmayer, M. Lanius, M. Luysberg, J. Doležal, E. Neumann, V. Cherepanov, I. Oštádal, G. Mussler, D. Grützmacher, and B. Voigtländer, *Physical Review B* **96** (2017), 10.1103/physrevb.96.035301.
- [12] D. Kim, S. Cho, N. P. Butch, P. Syers, K. Kirshenbaum, S. Adam, J. Paglione, and M. S. Fuhrer, *Nature Physics* **8**, 460 (2012).
- [13] F. Yang, A. A. Taskin, S. Sasaki, K. Segawa, Y. Ohno, K. Matsumoto, and Y. Ando, *ACS Nano* **9**, 4050 (2015).
- [14] C. E. ViolBarbosa, C. Shekhar, B. Yan, S. Ouardi, E. Ikenaga, G. H. Fecher, and C. Felser, *Physical Review B* **88** (2013), 10.1103/physrevb.88.195128.
- [15] F. Lüpke, S. Just, M. Eschbach, T. Heider, E. Młyńczak, M. Lanius, P. Schüffegen, D. Rosenbach, N. von den Driesch, V. Cherepanov, G. Mussler, L. Plucinski, D. Grützmacher, C. M. Schneider, F. S. Tautz, and B. Voigtländer, *npj Quantum Materials* **3** (2018), 10.1038/s41535-018-0116-1.
- [16] M. Lanius, J. Kampmeier, S. Kölling, G. Mussler, P. Koenraad, and D. Grützmacher, *Journal of Crystal Growth* **453**, 158 (2016).
- [17] A. Koma, *Thin Solid Films* **216**, 72 (1992).
- [18] S. Borisova, J. Krumrain, M. Luysberg, G. Mussler, and D. Grützmacher, *Crystal Growth & Design* **12**, 6098 (2012).
- [19] F. Lüpke, S. Korte, V. Cherepanov, and B. Voigtländer, *Review of Scientific Instruments* **86**, 123701 (2015).
- [20] J. Homoth, M. Wenderoth, T. Druga, L. Winking,

- R. G. Ulbrich, C. A. Bobisch, B. Weyers, A. Bannani, E. Zubkov, A. M. Bernhart, M. R. Kaspers, and R. Möller, *Nano Letters* **9**, 1588 (2009).
- [21] T. Tanikawa, I. Matsuda, T. Kanagawa, and S. Hasegawa, *Physical Review Letters* **93** (2004), 10.1103/physrevlett.93.016801.
- [22] F. Lüpke, J. Doležal, V. Cherepanov, I. Ošt'ádal, F. S. Tautz, and B. Voigtländer, *Surface Science* **681**, 130 (2019).
- [23] F. Lüpke, M. Eschbach, T. Heider, M. Lanius, P. Schüffelgen, D. Rosenbach, N. von den Driesch, V. Cherepanov, G. Mussler, L. Plucinski, D. Grützmacher, C. M. Schneider, and B. Voigtländer, *Nature Communications* **8**, 15704 (2017).
- [24] S. Bauer and C. A. Bobisch, *Nature Communications* **7**, 11381 (2016).
- [25] H. D. Li, Z. Y. Wang, X. Kan, X. Guo, H. T. He, Z. Wang, J. N. Wang, T. L. Wong, N. Wang, and M. H. Xie, *New Journal of Physics* **12**, 103038 (2010).
- [26] Y. Sakamoto, T. Hirahara, H. Miyazaki, S. ichi Kimura, and S. Hasegawa, *Physical Review B* **81** (2010), 10.1103/physrevb.81.165432.
- [27] T. Hirahara, Y. Sakamoto, Y. Takeichi, H. Miyazaki, S. ichi Kimura, I. Matsuda, A. Kakizaki, and S. Hasegawa, *Physical Review B* **82** (2010), 10.1103/physrevb.82.155309.
- [28] N. Bansal, Y. S. Kim, E. Edrey, M. Brahlek, Y. Horibe, K. Iida, M. Tanimura, G.-H. Li, T. Feng, H.-D. Lee, T. Gustafsson, E. Andrei, and S. Oh, *Thin Solid Films* **520**, 224 (2011).
- [29] R. D. Bringans and M. A. Olmstead, *Physical Review B* **39**, 12985 (1989).
- [30] S. Wu, Y. Zhou, Q.-H. Wu, C. Pakes, and Z.-Z. Zhu, *Chemical Physics* **382**, 41 (2011).
- [31] L. He, F. Xiu, Y. Wang, A. V. Fedorov, G. Huang, X. Kou, M. Lang, W. P. Beyermann, J. Zou, and K. L. Wang, *Journal of Applied Physics* **109**, 103702 (2011).
- [32] See Supplementary Material [url] for further details and examples about the general mechanism of band-bending in topological insulator materials.
- [33] H. Lüth, *Solid Surfaces, Interfaces and Thin Films*, 6th ed. (Springer Verlag, Heidelberg, 2015).
- [34] A. Many, Y. Goldstein, and N. Grover, *Semiconductor Surfaces* (North Holland, Amsterdam, 1965).
- [35] K. S. Novoselov, A. K. Geim, S. V. Morozov, D. Jiang, M. I. Katsnelson, I. V. Grigorieva, S. V. Dubonos, and A. A. Firsov, *Nature* **438**, 197 (2005).
- [36] T. Heinzel, *Mesoscopic Electronics in Solid State Nanostructures*, 3rd ed. (Wiley-VCH Verlag, Weinheim, 2010).
- [37] T. Arakane, T. Sato, S. Souma, K. Kosaka, K. Nakayama, M. Komatsu, T. Takahashi, Z. Ren, K. Segawa, and Y. Ando, *Nature Communications* **3** (2012), 10.1038/ncomms1639.
- [38] M. Bianchi, D. Guan, S. Bao, J. Mi, B. B. Iversen, P. D. King, and P. Hofmann, *Nature Communications* **1**, 128 (2010).
- [39] P. D. C. King, R. C. Hatch, M. Bianchi, R. Ovsyannikov, C. Lupulescu, G. Landolt, B. Slomski, J. H. Dil, D. Guan, J. L. Mi, E. D. L. Rienks, J. Fink, A. Lindblad, S. Svensson, S. Bao, G. Balakrishnan, B. B. Iversen, J. Osterwalder, W. Eberhardt, F. Baumberger, and P. Hofmann, *Physical Review Letters* **107** (2011), 10.1103/physrevlett.107.096802.
- [40] H. M. Benia, C. Lin, K. Kern, and C. R. Ast, *Physical Review Letters* **107** (2011), 10.1103/physrevlett.107.177602.
- [41] D. Kong, J. J. Cha, K. Lai, H. Peng, J. G. Analytis, S. Meister, Y. Chen, H.-J. Zhang, I. R. Fisher, Z.-X. Shen, and Y. Cui, *ACS Nano* **5**, 4698 (2011).
- [42] J. G. Analytis, J.-H. Chu, Y. Chen, F. Corredor, R. D. McDonald, Z. X. Shen, and I. R. Fisher, *Physical Review B* **81** (2010), 10.1103/physrevb.81.205407.
- [43] M. Brahlek, N. Koirala, N. Bansal, and S. Oh, *Solid State Communications* **215-216**, 54 (2015).
- [44] M. Brahlek, N. Koirala, M. Salehi, N. Bansal, and S. Oh, *Physical Review Letters* **113** (2014), 10.1103/physrevlett.113.026801.
- [45] J. Zhang, C.-Z. Chang, Z. Zhang, J. Wen, X. Feng, K. Li, M. Liu, K. He, L. Wang, X. Chen, Q.-K. Xue, X. Ma, and Y. Wang, *Nature Communications* **2** (2011), 10.1038/ncomms1588.
- [46] Y. Satake, J. Shiogai, D. Takane, K. Yamada, K. Fujiwara, S. Souma, T. Sato, T. Takahashi, and A. Tsukazaki, *Journal of Physics: Condensed Matter* **30**, 085501 (2018).
- [47] J. Kellner, M. Eschbach, J. Kampmeier, M. Lanius, E. Młyńczak, G. Mussler, B. Holländer, L. Plucinski, M. Liebmann, D. Grützmacher, C. M. Schneider, and M. Morgenstern, *Applied Physics Letters* **107**, 251603 (2015).